



Article

# Study on Bearing Capacity of Honeycomb Sandwich Structure Embedded Parts

Wei Sun<sup>1</sup>, Junyi Xiao<sup>2</sup> , Xuanwei Hu<sup>2</sup> , Baoxin Hao<sup>1</sup>, Huan Zhang<sup>1</sup>, Peng Zhang<sup>1</sup>, Tianhe Gao<sup>2</sup> and Kuo Tian<sup>2,\*</sup>

<sup>1</sup> Institute of Spacecraft System Engineering, China Academy of Space Technology, Beijing 100094, China; sunwei2@mail.dlut.edu.cn (W.S.)

<sup>2</sup> State Key Laboratory of Structural Analysis, Optimization and CAE Software for Industrial Equipment, Dalian University of Technology, Dalian 116024, China; dk22706042@mail.dlut.edu.cn (J.X.); 2901197508@mail.dlut.edu.cn (X.H.)

\* Correspondence: tiankuo@dlut.edu.cn

**Abstract:** In the composite structure of spacecraft, the honeycomb sandwich structure is the basic bearing component used to bear and transmit loads. To explore the influencing factors on the bearing capacity of honeycomb sandwich structures, this study combines local tests and speckle measurement systems to conduct tensile tests on 10 test specimens with different parameters. Firstly, a comprehensive assessment was conducted on the accuracy of the loading and measurement system, the rationality of the testing method, and the mechanical properties of the test piece. It was found that the maximum measurement error of the speckle measurement system did not exceed 0.01 mm, and the differences between the yield load and failure load measured using different inner diameters of the compression ring were 0.15% and 3.84%, respectively. This indicates that the measurement system is accurate and that the influence of the inner diameter of the compression ring can be ignored. Moreover, it was found that considering the accuracy retention ability of the structure under load, the allowable load of the embedded parts is about 90% of the yield load. Finally, the data of specimens with different parameters were compared and it was found that the strength of the honeycomb sandwich structure is directly proportional to the thickness of the skin, the density of the honeycomb core cells, and the size of the embedded parts.

**Keywords:** honeycomb sandwich structure; embedded parts; bearing capacity; influencing factor



**Citation:** Sun, W.; Xiao, J.; Hu, X.; Hao, B.; Zhang, H.; Zhang, P.; Gao, T.; Tian, K. Study on Bearing Capacity of Honeycomb Sandwich Structure Embedded Parts. *J. Compos. Sci.* **2023**, *7*, 281. <https://doi.org/10.3390/jcs7070281>

Academic Editor: Francesco Tornabene

Received: 6 June 2023

Revised: 2 July 2023

Accepted: 5 July 2023

Published: 8 July 2023



**Copyright:** © 2023 by the authors. Licensee MDPI, Basel, Switzerland. This article is an open access article distributed under the terms and conditions of the Creative Commons Attribution (CC BY) license (<https://creativecommons.org/licenses/by/4.0/>).

## 1. Introduction

Sandwich composite structures have a wide range of applications in aerospace [1–3], such as the secondary structure of aircraft, cabin components, landing gear flaps, engine nacelles, etc. Sandwich composite structures usually consist of two high-strength panels and a low-density core structure in the middle. The sandwich structures investigated in this paper are honeycomb sandwich structures, which means the core structure in the middle has a honeycomb form.

The honeycomb sandwich structure can carry bending moments and axial forces effectively while greatly reducing the weight of the structure, which results in the organic combination of strength and lightweight design. However, honeycomb sandwich structures still have weaknesses in terms of connectivity. To reduce weight, the core of the honeycomb sandwich structure is usually light, soft, and weak [4], which cannot directly support mechanical connections. Thus, sufficiently strong connecting parts are required. In response to this problem, embedded parts such as metal fasteners are often adopted, which in turn enable the transfer of load to the external connection apparatus. To install these embedded parts, honeycomb sandwich structures often use potting materials acting as a support to reinforce the core. Honeycomb sandwich structures are particularly susceptible to damage by local loads, and stress concentrations near the embedded parts should receive special

attention during the reinforcement design of sandwich panels [1,5,6]. Thus, it is particularly important to study the factors influencing the pull-off force on the embedded parts.

Extensive research has been conducted by multiple scholars on sandwich structures. Thomsen et al. [7] proposed a mathematical model to analyze sandwich-embedded parts with elastic faces of honeycomb cores, focusing on the effectiveness of the potting method. Demelio et al. [8] studied the fatigue strength of sandwich structures with Kevlar/Epoxy composite surfaces, Nomex cores, and rivets inserted. Yeh et al. [9] tested and analyzed the strength of bolted connections of composite sandwich T-shaped embedded parts. However, due to the limitations of the traditional measuring method using strain gauge sensors, the heavy patching work and the lack of measurement accuracy make this type of test extremely difficult.

The digital speckle correlation method (DSCM) is a recently emerging concept gradually gaining attention among researchers as an advanced technique for experimental stress analysis [10]. DSCM is a non-contact, high-speed method with high accuracy, simple operation and no special requirements for the test environment. It allows 3D full-field data measurement of the deformation of materials and structures. In speckle measurement, the light source irradiates the surface of the object to be measured and produces speckles, which are reflected or transmitted by the surface of the object and then converge again on the imaging surface. Since the optical wave undergoes phase distortion when passing through the medium, a complex interference pattern is produced on the imaging surface. By analyzing the interference pattern, information on the deformation of the object during the test can be calculated. DSCM can determine the full-field displacement by comparing speckle images before and after deformation. The main principle is to obtain accurate measurements of 3D coordinates, displacement, and strain of the object surface during deformation by obtaining digital speckle images of the surface before and after deformation through the binocular stereo vision method [11].

DSCM has been widely used for mechanical analysis of materials, for example, in studies of strain concentration in composites and cracks sprouting in different materials [12,13], deformation measurements, and nondestructive measurements [14–16]. Jin et al. [17] studied the basic principles of DSCM and its measurement accuracy. Broggiato et al. [12] used 2D DSCM to measure strain in composite materials. Yao et al. [13] studied the deformation measurement of composite pressure vessels using 2D DSCM. It can be seen that DSCM is an effective method to measure the full-field mechanical response of the test specimen during testing, which is the reason DSCM is adopted as the measurement system in this paper.

DSCM is mainly adopted to analyze and process final test results. Zamani et al. [18] assessed the strain fields and damage evolution of rock cores under real-time flexural loading conditions using DSCM analysis. The experimental results and DSCM analysis were validated by a three-dimensional finite element analysis considering elastoplastic behavior and the possibility of crack growth. Giordano et al. [19] loaded a composite sandwich structure, composed of carbon fiber woven face sheets and a relatively compliant foam core, in three-point bending. Images of the specimen before and after deformation were captured and analyzed using a DSCM program. Li et al. [20] fixed both ends of a sandwich panel in custom fixtures, with the top fixture applying an axial compression load to the structure and the bottom fixture completely securing the end. The structural deformation behavior was captured using digital speckle correlation technology.

In summary, to explore the influencing factors on the bearing capacity of embedded components in honeycomb sandwich structures, this article adopts a local test method based on the DSCM system to investigate the effects of different skin thicknesses, honeycomb core heights, and other factors on the bearing capacity of honeycomb sandwich structure cores. The rest of this paper is organized as follows. In Section 2, the testing process and methods for the bearing capacity of the embedded components in honeycomb sandwich structures are described in detail. In Section 3, the experimental process and results are reported in detail. The conclusion of this work is given in Section 4.

## 2. Experimental Method

### 2.1. Introduction to Test Specimens

Firstly, we briefly introduce the condition of the honeycomb panel specimen. The skin material of the specimen is aluminum alloy 2A12, and the embedded parts are aluminum alloy general M4 pre-embedded parts and special M4 pre-embedded parts. The thickness of the honeycomb core is classified as 14.4 mm, 20.1 mm, 25 mm, and 29.4 mm, while the thickness of the skin is classified as 0.3 mm and 0.5 mm. The honeycomb core specifications are LF2-YH0.03 × 5, LF2-YH0.03 × 4, and LF2-YH0.03 × 3. Taking LF2-YH0.03 × 5 as an example, LF2 indicates that the honeycomb core material is LF2 aluminum alloy. YH0.03 × 5 refers to the size of the cell core; that is, the thickness of the cell core is 0.03 mm, and the side length of the cell core is 4 mm. The overall size of the honeycomb panel specimen is 300 × 300 mm. Figure 1 and Table 1 show the differences between the special embedded parts and standard embedded parts. Special embedded parts can be divided into two types: thin column embedded parts and deep flange embedded parts. The adhesive film also has different varieties, and there are different ranges of foam filling as well. The different combinations of these parameters lead to 15 kinds of specimens, as shown in Tables 2 and 3.

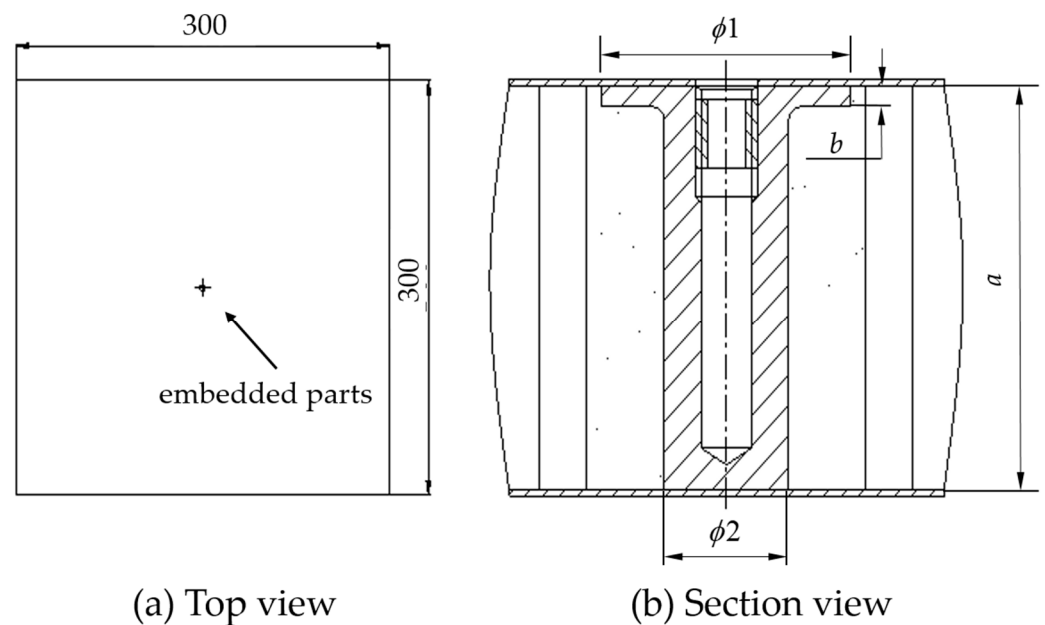


**Figure 1.** Schematic diagram of assembly relationship and dimension parameters of honeycomb sandwich board and embedded parts. (a) Top view. (b) Section view.

**Table 1.** Parameter description in Figure 1.

	$\phi 1$ (mm)	$\phi 2$ (mm)	$a$ (mm)	$b$ (mm)
Deep flange	25	10	$29.4_{-0.1}^{\circ}$	1.5
General	20	10	$29.4_{-0.1}^{\circ}$	1.5
Thin column	20	8	$29.4_{-0.1}^{\circ}$	1.5

**Table 2.** Code for ranges of foaming adhesive in Table 2.

Ranges of Foaming Adhesive	Code
Conventional process (Wrap to the flanged edge)	A
Conventional process (Wrap the foaming adhesive around)	B
1 circle more than normal is filled around the embedded parts	C
2 circles more than normal are filled around the embedded parts	D

**Table 3.** State and quantity description of the test specimens.

Serial Number of the Experimental Set	Thickness of the Honeycomb Core	Thickness of the Skin	Core Specifications	Pre-Embedded Parts	Ranges of Foaming Adhesive	Quantity
SYJ0-1~9	29.4 mm	0.3 mm	H0.03 × 5	General	A	9
SYJ1-1~9	14.4 mm	0.3 mm	H0.03 × 5	General	A	9
SYJ2-1~9	20.4 mm	0.3 mm	H0.03 × 5	General	A	9
SYJ3-1~9	25.0 mm	0.3 mm	H0.03 × 5	General	A	9
SYJ4-1~9	29.4 mm	0.5 mm	H0.03 × 5	General	A	9
SYJ5-1~9	29.4 mm	0.3 mm	H0.03 × 4	General	A	9
SYJ6-1~9	29.4 mm	0.3 mm	H0.03 × 3	General	A	9
SYJ7-1~9	29.4 mm	0.3 mm	H0.03 × 5	General	A	9
SYJ8-1~9	29.4 mm	0.3 mm	H0.03 × 5	Deep flange	A	9
SYJ9-1~9	29.4 mm	0.3 mm	H0.03 × 5	No flange	B	9
SYJ10-1~9	29.4 mm	0.3 mm	H0.03 × 5	Thick column	A	9
SYJ11-1~9	29.4 mm	0.3 mm	H0.03 × 5	Thin column	A	9
SYJ12-1~9	29.4 mm	0.3 mm	H0.03 × 5	General	C	9
SYJ13-1~9	29.4 mm	0.3 mm	H0.03 × 5	General	D	9
SYJ14-1~9	29.4 mm	0.3 mm	H0.03 × 5	Shallow flange	A	9
Total	—	—	—	—	—	135

*2.2. Introduction to the Loading and Measurement State of the Test Specimen*

The pull-out force load was applied to the embedded part, which was perpendicular to the direction of the panel surface, to assess the pull-out strength of the embedded parts. The fixture and loading method of the specimen are shown in Figure 2. During the pull-out test, the specimen was fixed with a compression ring and the axial load was applied through screws. To study the influence of different inner diameters of the compression ring on the bearing capacity, two types of compression rings with inner diameters of Φ100 and Φ200 were constructed. The Φ100 compression ring had a thickness of 15 mm and was made of aluminum alloy, while the Φ200 compression ring had a thickness 8 mm and was made of steel. The reason for using different materials in the test was to further verify that the pressure ring parameters, including the material and inner diameter, have less influence on the bearing capacity. A further reason was to provide design ideas for the subsequent practice of the pressure ring, which is explained further below.

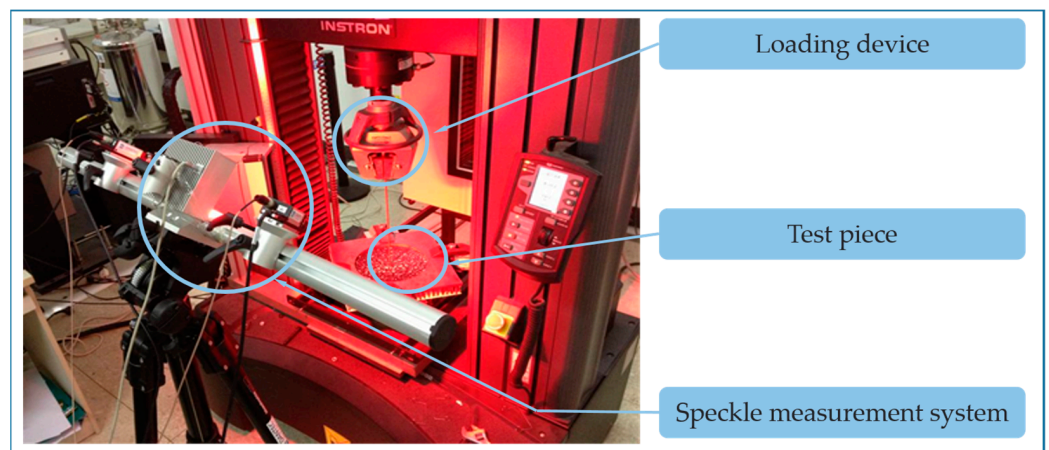


**Figure 2.** Pull-off test loading state (using electronic universal testing machine and Q400 measuring system).

Real-time load-displacement curves were obtained using an electronic universal testing machine to load the specimen axially and continuously at a loading rate of 1 mm/min. During the loading process, the full-field speckle deformation measurement system was used to monitor the full-field displacement and strain within a radius of 180 from the loading point on the loading surface. The main equipment and instruments used in the test are shown in Table 4.

**Table 4.** Main equipment and instruments required for the test.

Instrument Name	Type	Manufacturers	Specification	Quantity
Electronic universal testing machines (UTM)	5982	INSTRON Inc (Norwood, MA, USA)	Grade 0.5	1
Speckle measurement system (SMS)	Q400	DANTE GMBH (Regensburg, Germany)	1 μm	1

To remove the gap in the loading system and ensure the coincidence of measurement data, the specimen was first pre-applied with a 100 N axial load before the formal test, and the data of the measurement system were reset to zero under this load.

2.3. Test Contents and Sequence

In addition, to comprehensively evaluate the accuracy of the loading and measuring system, the rationality of the test method, and the mechanical properties of the test specimen, some experimental exploration and pre-experiments were required. A flow chart for the research on the bearing capacity of embedded parts in honeycomb sandwich structure is shown in Figure 3. It mainly includes two parts: pre-experiments and formal testing.

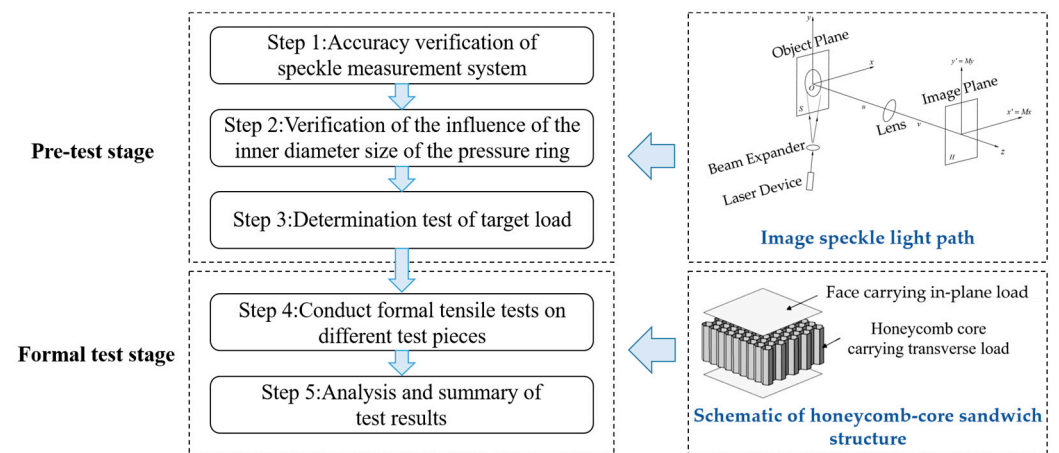


**Figure 3.** Flow chart for research on the bearing capacity of embedded parts in honeycomb sandwich structure.

Pre-test section:

Step 1: Verification of the accuracy of the speckle measurement system.

The speckle measurement system has proven to be effective in accurately assessing stress changes in structural plates before damage occurs to the embedded parts. This method offers multiple advantages, including high accuracy, high sensitivity, and non-contact measurements. To confirm the accuracy of the displacement measurement provided by the speckle measurement system, the results obtained with this system were compared with those from the displacement measurement system on the testing machine. Firstly, we fixed the specimen with the loading bar and cleared the displacement measurement data of the displacement measurement system of the testing machine and the speckle measurement system. Then, we used the testing machine to move the specimen along the longitudinal direction. Next, at a selected moment during the movement of the specimen, the displacement of the test specimen was measured simultaneously using the displacement measurement system and the speckle measurement system. The speckle measurement

method optically tracks the deformation process of the speckle pattern on the surface of the object and calculates the change in the gray value of the speckle domain to obtain the deformation and strain data of the measured area of the test specimen. Finally, the displacement results obtained by the two measurement systems were compared, and it was determined according to the prediction error whether the accuracy of the speckle measurement system met the requirements.

Step 2: Verification of the effect of the inner diameter size of the compression ring.

The test specimens SYJ5-1 and SYJ5-2 were selected and fixed with the compression ring with an inner diameter is  $\Phi 200$ . The tensile load was increased in one direction until failure to determine the yield load and failure load of the test specimens. By comparing the two sets of data, we analyzed the influence of the inner diameter of the compression ring on the average yield load and failure load obtained from the test, and judged the influence of the change of the inner diameter on the bearing capacity of the test specimens.

Step 3: Test to determine target load.

The test specimens SYJ4-1 and SYJ4-2 were selected and fixed with the compression ring with an inner diameter is  $\Phi 200$ . The tensile load was increased in one direction until failure to determine the yield load and failure load of the test specimens. The 90% and 80% levels of the lowest yield load were taken as the target loads for SYJ4-3 and SYJ4-4, respectively, and the SYJ4-3 and SYJ4-4 specimens were loaded and unloaded once. We observed the overlap of loading and unloading curves and the residual displacement after unloading. Then, 120% of the lowest yield load was taken as the target load, and SYJ4-4 was loaded and unloaded once to again observe the overlap of the loading and unloading curves.

Comparing the test results above, the load of the honeycomb panel embedded parts can be judged. The target loads of the following test pieces were then determined according to this ratio. After loading and unloading the test specimens once, the tensile load was increased in one direction until failure.

Formal test section:

Step 4: Formal test.

Since the ratio of the target load to the yield load was determined in the tests of SYJ4-1 and SYJ4-4, the respective target loads of other test specimens could be determined according to this ratio. The first and second pieces were subjected to a one-way increase in load, directly to failure, to determine the yield load and failure load of the test specimens. Then the target load for each test specimen was calculated based on the minimum yield load and the ratio determined above. The remaining test specimens were loaded and unloaded once, and the overlap of the loading and unloading curves during the test were checked. After loading and unloading, the tensile load was increased in one direction until failure.

Step 5: Analysis of test results.

The final failure modes of each test specimen were observed and the failure mechanisms of the embedded parts were summarized. Then, we analyzed the experimental data obtained from the speckle measurement system to draw experimental conclusions.

### 3. Results

#### 3.1. Analysis of Pre-Experiment Results

Firstly, the accuracy of the speckle measurement system was verified. The test specimen SYJ5-1 was selected, and the displacement measurement system and speckle measurement system of the testing machine were used to measure the displacement of the test specimen. Five sets of test data were obtained, as shown in Table 5. It can be seen that the displacement measurement results obtained by the two methods match very well, with a maximum error of less than 0.01 mm, which indicates that the accuracy of the speckle measurement system can meet the requirements.

**Table 5.** Comparison of the data from UTM and SMS.

Displacement Measured by the UTM (mm)	Displacement Measured by the SMS (mm)	Maximum Deviation (mm)
5.001	5.0002	0.0008
6.001	6.0054	0.0044
6.998	7.0055	0.0075
8.001	8.0086	0.0076
9.001	9.0092	0.0082

Next, the results from the test of the pressure ring’s inner diameter influence were analyzed. The test specimens SYJ5-1 and SYJ5-2 were selected and fixed with the compression ring with an inner diameter of  $\Phi 100$ . The tensile load was increased in one direction until failure to determine the yield load and failure load of the test specimens. The two sets of data were compared, as shown in Table 6. It can be seen that the average yield loads obtained by the tests were the same and the differences in failure loads for different inner diameters of the pressure rings were very small, which shows that different inner diameters of the pressure ring have little effect on the load capacity of the structure. In the tensile tests of the other test specimens, all the test specimens were fixed with compression rings of  $\Phi 200$  inner diameter.

**Table 6.** Test data on influence of different inner diameters of pressure ring on tensile strength.

Inner Diameter	Test Specimen Number	Yield Load (N)	Fracture Load (N)
$\Phi 200$	SYJ5-1	2057	5263
	SYJ5-2	2037	5246
	Average	2047	5255
$\Phi 100$	SYJ5-3	2281	5891
	SYJ5-4	1818	5038
	Average	2050	5465
Average bearing capacity deviation of two pressure ring states (%)		0.15	3.84

Finally, the deterministic test results of the target load were analyzed. Firstly, the test specimens SYJ4-1 and SYJ4-2 were selected. The tensile load was increased in one direction to directly cause failure at yield loads of 1249 N and 1558 N and failure loads of 6634 N and 7312 N for the two test specimens, respectively. The 90% level of the lowest yield load (1249 N) of the two (i.e., 1124 N) was taken as the target load. Then SYJ4-3 was loaded and unloaded once. As shown in Figure 4, it can be seen that the overlap of loading and unloading curves is good. The residual displacement after unloading was 0.085 mm. General honeycomb panel design requires 0.1 mm/100 mm  $\times$  100 mm surface flatness for equipment installation. The residual displacement was less than 0.1 mm, which meets the general design requirements.

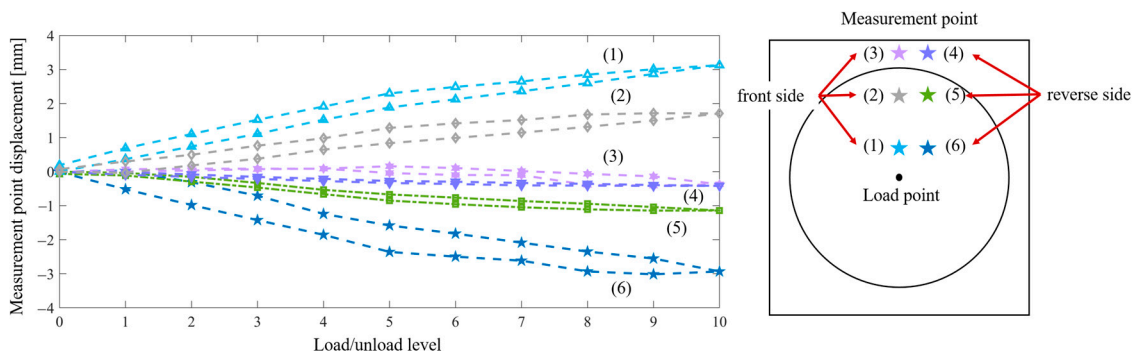


**Figure 4.** Schematic diagram of loading and unloading curve for points with large displacement.

To fully verify the deformation recovery capacity of the honeycomb panel embedded parts under different proportions of target loads, 80% of the lowest yield load (1249 N), i.e., 999 N, was taken as the target load, and SYJ4-4 was loaded and unloaded once. It can be seen that the overlap of loading and unloading curves was good. The residual displacement after unloading was 0.059 mm, which meets the design requirements. The residual displacement was smaller than the state where the target load was 90% of the yield load, which indicates that the deformation recovery of the honeycomb panel embedded parts is better under the lesser load.

To fully verify the deformation recovery capacity of the honeycomb panel embedded parts under different proportions of target loads, 120% of the lowest yield load (1249 N), i.e., 1499 N, was taken as the target load, and SYJ4-4 was loaded and unloaded once again. It can be seen that the overlap of loading and unloading curves is not good. After unloading, the embedded parts were observed with the naked eye. A small protrusion deformation was observed in the local area of the embedded parts. The residual displacement was 0.112 mm, which does not meet the design requirements.

In summary, it is more appropriate to set the use load of the honeycomb plate as 90% of the yield load. The target loads of the test specimens were all determined according to this ratio. After loading and unloading, the tensile load was increased in one direction until failure.

### 3.2. Analysis of Failure Forms of Honeycomb Structure in Formal Tests

In order to fully understand the failure mechanism of the embedded parts, after the test was completed, two specimens were taken for each kind of test specimen, corresponding to the maximum yield load and the maximum failure load, respectively. The specimens were cut along the centerline of the embedded part to observe the internal damage and compared with other specimens that were not subjected to loading. Due to the aluminothermic reaction, cutting fluid cannot be used in honeycomb panel cutting. In order to ensure accuracy and internal structure, the disc-cutting method was adopted, and the final cutting flatness and smoothness were both good. The results are shown in Figures 5 and 6. There are two forms of the final failure in the test specimens: collapse and cracking of the honeycomb core after loading (as shown in Figures 5b and 6b), and skin adhesive interface cracking of the honeycomb core after loading (as shown in Figures 5c and 6c). The specific information for the standard test specimens is shown in Tables 7 and 8, and the comparison results of all test specimens are shown in Table 9.

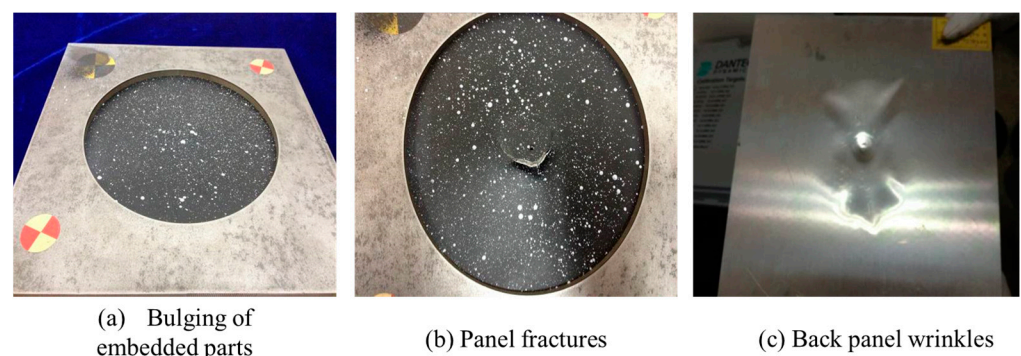


**Figure 5.** Schematic diagram of typical failure modes of test pieces under tensile load. (a) Bulging of embedded parts. (b) Panel fractures. (c) Back panel wrinkles.

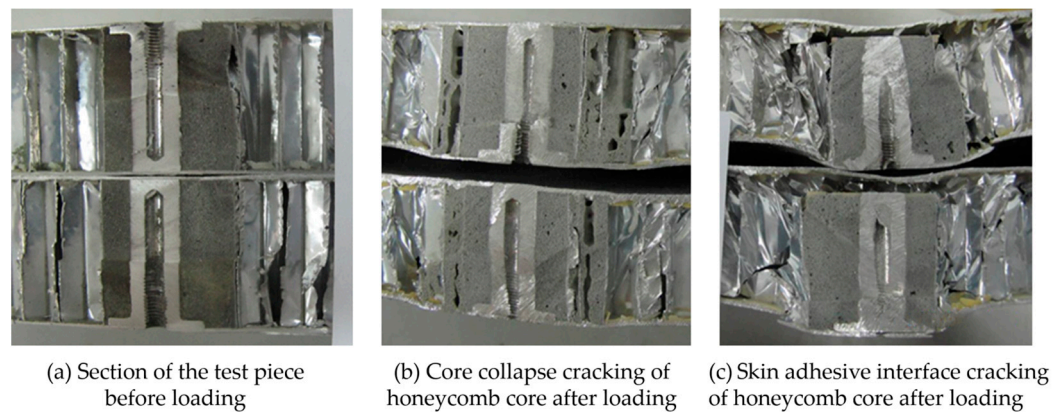


**Figure 6.** Typical sections of the test pieces after tensile failure. (a) Section of the test piece before loading. (b) Core collapse cracking of honeycomb core after loading. (c) Skin adhesive interface cracking of honeycomb core after loading.

**Table 7.** Code for the cut sections in Table 8.

The Cut Section	Code
The joint between the embedded part and the adhesive is cracked	$\alpha$
The honeycomb core is collapsed and cracked	$\beta$

**Table 8.** Tensile failure load test data of standard test specimen honeycomb plate embedded parts.

Test Specimen Name	Test Specimen Number	Target Load (N)	Residual Displacement after Loading and Unloading (mm)	Yield Load (N)	Fracture Load (N)	Failure Mode	Cut Section
Standard component	SYJ-0-1	-	-	1540	6193	Embedment bulking	$\alpha$
	SYJ-0-2	-	-	1577	6222	Embedment bulking	-
	SYJ-0-4	1386	0.21	1395	6043	Embedment bulking	-
	SYJ-0-5	1100	0.07	1406	5380	Embedment bulking	-
	SYJ-0-6	1100	0.09	1181	6138	Embedment bulking	-
	SYJ-0-7	1100	0.06	1185	5978	Embedment bulking	$\alpha$
	SYJ-0-8	1100	0.04	1171	6635	Embedment bulking	$\beta$
	SYJ-0-9	1100	0.08	1143	5779	Embedment bulking	$\beta$
	Average	—	—	1247	5992	The recommended allowable load is 1100 N	

**Table 9.** Tensile failure load test data of various honeycomb plate embedded parts.

Test Part Name	Test Specimen Number	Average Yield Load (N)	Average Fracture Load (N)	Recommended Allowable Load (N)
Standard component	SYJ-0-1~9	1247	5992	1100
Specimen with thickness 15	SYJ-1-1~9	599	4926	500
Specimen with thickness 21	SYJ-2-1~9	649	5487	600
Specimen with thickness 25	SYJ-3-1~9	886	4630	800
Specimen with panel thickness 0.5	SYJ-4-1~9	1684	6421	1120
4-Honeycomb lattice component	SYJ-5-1~9	1700	4786	1500
5-Honeycomb lattice component	SYJ-10-3~9	1271	4973	1250
Thick column component	SYJ-11-1~9	1119	>6100	1000
Less-foaming adhesive component	SYJ-12-1~9	1509	>6100	1400
Much-foaming adhesive component	SYJ-13-1~9	2151	>6100	2000

As stated above, the observed internal damage included two types: honeycomb core collapse cracking; and embedded parts and skin adhesive interface cracking. As shown in Figures 5b and 6b, honeycomb core collapse cracking was prevalent and was the main

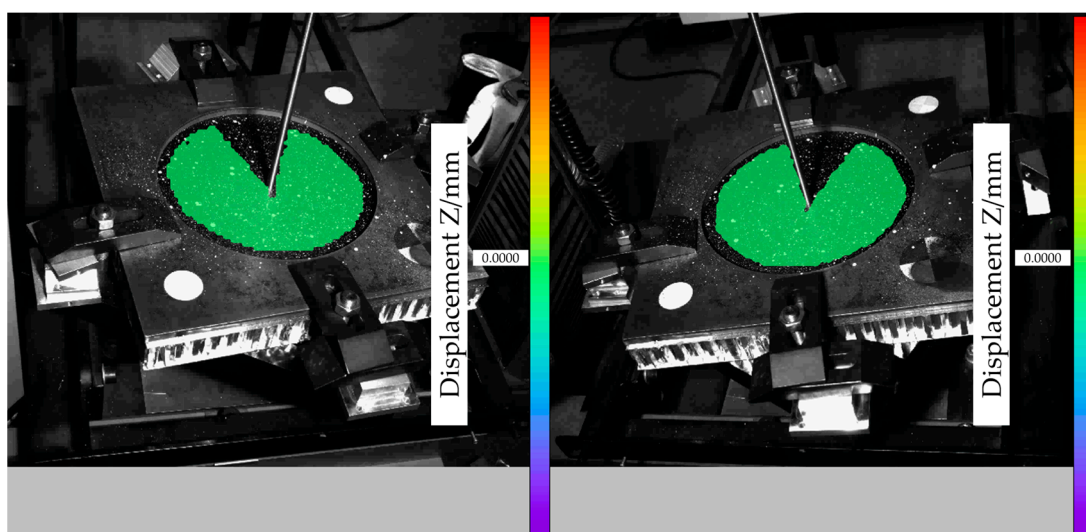
form of damage. As shown in Figures 5c and 6c, cracking of the embedded parts and skin adhesive interface were observed in the final stage of damage, which tended to occur after the honeycomb core collapsed and cracked. Components such as the body of the embedded parts, the thread of the embedded parts, the bonding between the embedded parts and the foam adhesive, and the bonding between the foam adhesive and the honeycomb core were not damaged, which indicates that the keys to the pull-out bearing capacity of the embedded parts are the shear strength of the core itself and the area of the bearing capacity, that is, the filling range of the foaming adhesive, whereas the strength of the skin, the embedded parts and the foaming adhesive itself do not play a role.

3.3. Analysis of Experimental Data Obtained by the Speckle Measurement System

In this test, the speckle measurement system was used for the first time to measure the displacement on the surface of the test specimen, and the typical displacement field distribution measured is shown in Figure 7. Based on the displacement data, the strain distribution of the honeycomb panel surface under different loads can be calculated. Typical strain results and stress calculation results are shown in Table 10. A typical strain field distribution is shown in Figure 8.

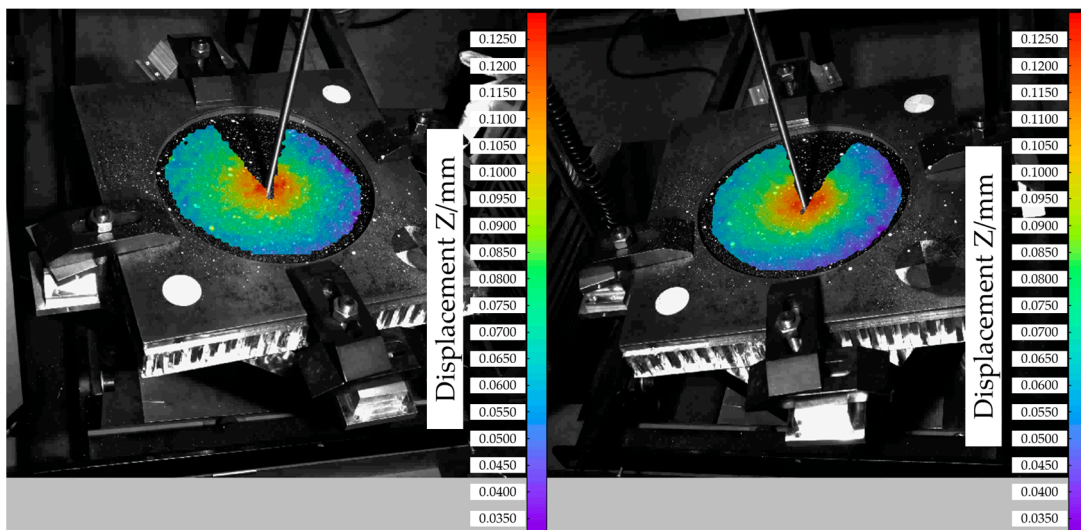
Table 10. Typical strain results and stress calculation results near the embedded parts measured by the SMS.

Test Specimen Number	Load (N)	First Principal Strain ( $\mu\epsilon$ )	Second Principal Strain ( $\mu\epsilon$ )	Von Mises Stress Obtained by Linear Calculation (MPa)
SYJ4-2	1558 (Yield)	2276	-276	163
	7312 (Fracture)	15,518	7289	1249
SYJ8-1	2355 (Yield)	3129	919	234
	5537 (Fracture)	25,722	4809	1858
SYJ10-8	1292 (Yield)	3739	-3096	313
	5169 (Fracture)	73,761	-10,951	5067
SYJ11-2	1485 (Yield)	497	-4879	335
	5994 (Fracture)	12,465	3189	921
SYJ14-7	955 (Yield)	1784	-4829	341
	3555 (Fracture)	14,404	-16,704	1423

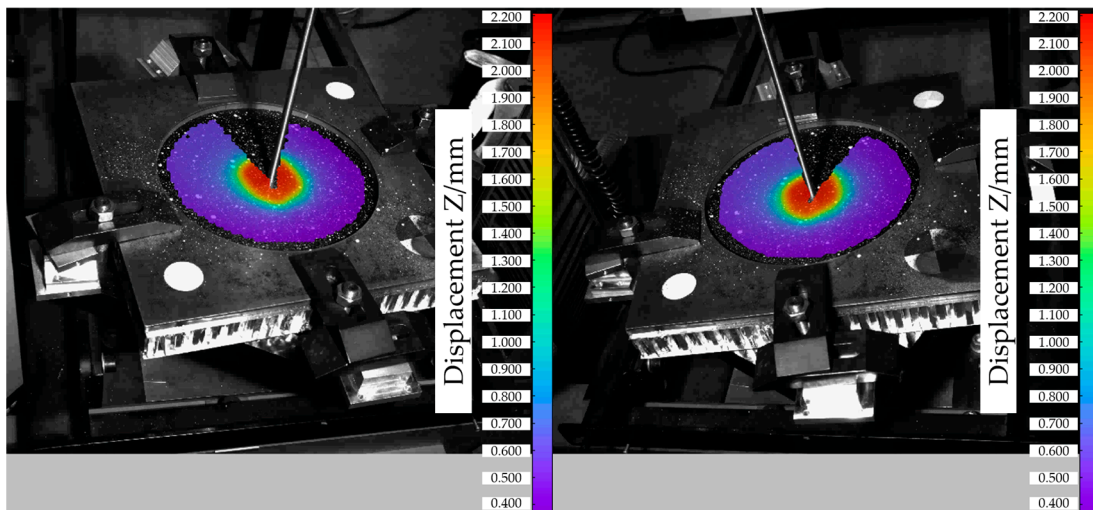


(a) Initial state displacement field view

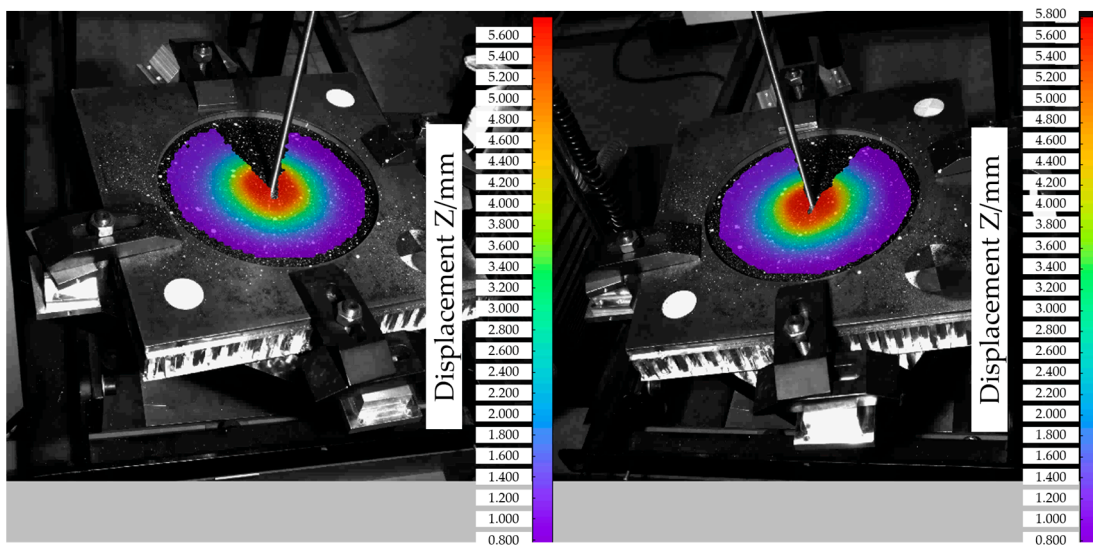
Figure 7. Cont.



(b) The displacement field view at about 0.1 mm stretching

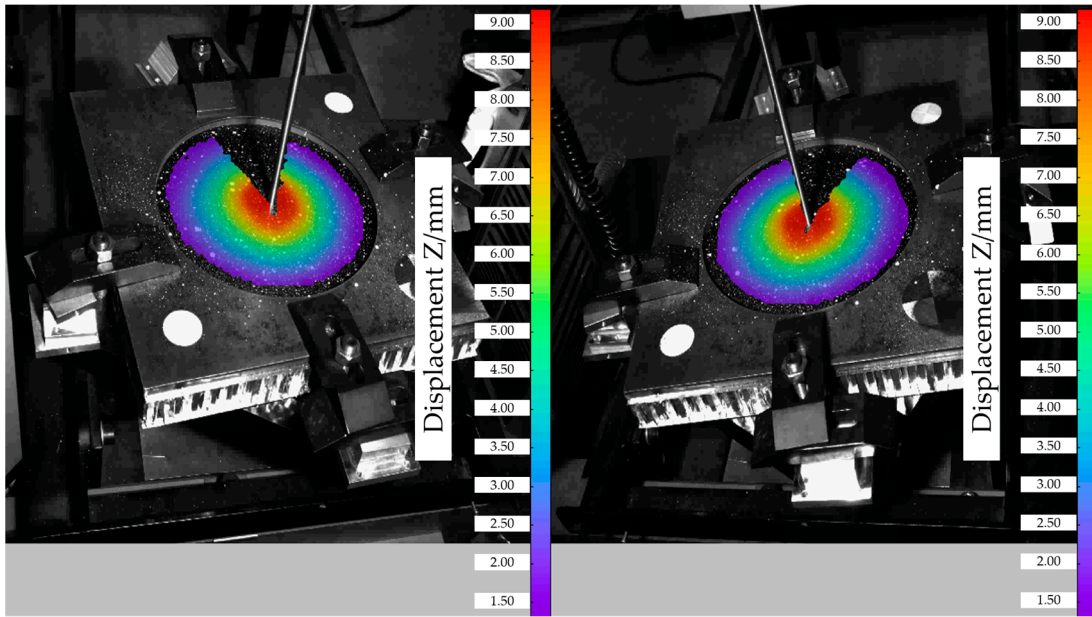


(c) The displacement field view at about 1 mm stretching



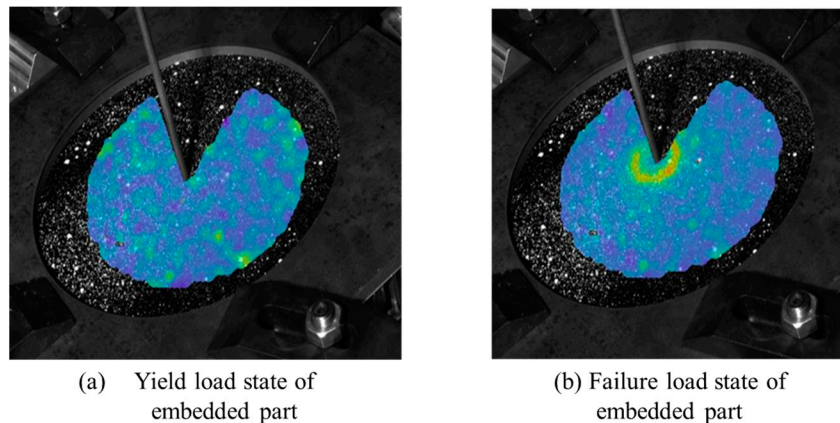
(d) The displacement field view at about 5 mm stretching

Figure 7. Cont.



(e) The displacement field view at about 10 mm stretching

**Figure 7.** Typical displacement distribution on the surface of the test specimens corresponding to different tensile loads. (a) Initial state displacement field view. (b) The displacement field view at about 0.1 mm stretching. (c) The displacement field view at about 1 mm stretching. (d) The displacement field view at about 5 mm stretching. (e) The displacement field view at about 10 mm stretching.



**Figure 8.** Typical strain field distribution on the surface of the test specimen corresponding to different tensile loads. (a) Yield load state of embedded part. (b) Failure load state of embedded part.

It can be seen that when an obvious yield appears on the load-displacement curve of the embedded part, the stress of the skin obtained by linear calculation also basically reaches the yield stress of the aluminum alloy material (260 MPa). In this state, local unrecoverable deformation begins to appear in the honeycomb panel. Thus, the allowable pulling load of the embedded parts should be slightly lower than the yield load.

Under the failure load of the embedded part, the local deformation of the skin was more than 10,000  $\mu\epsilon$ , and the stress had already exceeded the yield strength of the material. The embedded parts completely lost their bearing capacity with large deformation to a certain extent.

### 3.4. Summary and Discussion of Experimental Data

A pull-out force test of honeycomb sandwich structure embedded parts was carried out according to the "Pull-out Test Outline of Honeycomb Sandwich Structure Embedded Parts" procedure. The equipment used in the test functioned well. The test data were correct and valid. The findings from this experiment, which will help in the subsequent design of honeycomb panel embedded parts, can be summarized as follows.

1. Considering the precision maintenance ability of the structure after loading, the allowable load of the embedded parts is about 90% of the yield load.
2. The bearing capacity of the embedded parts is closely related to the height of the honeycomb core, which is basically a linear relationship. To improve the bearing capacity, increasing the thickness of the honeycomb core is an effective method.
3. Increasing the thickness of the honeycomb panel skin has little effect on the pull-out load capacity of the embedded parts.
4. The bearing capacity of the embedded parts is very closely related to the specification of the honeycomb core. The denser the honeycomb core, the higher the bearing capacity. To improve the bearing capacity, local encryption of honeycomb cores is an effective method.
5. Changing the honeycomb panel core adhesive film has little effect on the pull-out load capacity of the embedded parts.
6. The bearing capacity of embedded parts is closely related to their flanging size, which is basically linear. To improve the bearing capacity, increasing the flanging size of pre-embedded parts is an effective method.
7. The bearing capacity of the embedded parts has a certain relationship with the diameter of the pre-embedded column section. The larger the diameter of the column section, the higher the load capacity, but the impact is not significant. To improve the bearing capacity, increasing the diameter of the pre-embedded column section is not an effective method.
8. The bearing capacity of the embedded parts is closely related to the range of foaming adhesive filled around the pre-embedded parts. The larger the range of foaming adhesive filled around the pre-embedded parts, the higher the bearing capacity. To improve the bearing capacity, increasing the range of foaming adhesive filled around the embedded parts is an effective method.
9. Honeycomb core collapse cracking is the main form of damage. The key characteristics contributing to the pull-out bearing capacity of the embedded parts are the shear strength of the core itself and the area of the bearing capacity, that is, the filling range of the foaming adhesive. The pull-out bearing capacity has little relationship with the strength of the skin, the embedded parts or the foaming adhesive itself.
10. The data obtained from the test can be directly used for the strength design and calibration of the relevant embedded parts.

### 4. Conclusions

To investigate the influence of factors such as skin thickness and honeycomb core height on the load-bearing capacity of honeycomb sandwich structures, in this study, local experiments and speckle measurement systems were conducted on 15 test pieces representing different parameters. In the experiment, the accuracy of the speckle measurement system and the impact of the pressure ring size on the test results were first verified through pre-testing, and the target load of each test piece was determined. Then, formal tests were conducted to measure the yield load and failure load of different parameter test pieces, and finally, the failure mechanisms of the embedded parts were summarized.

During the experiment, the speckle measurement system was able to observe the local full-field mechanical response, which is of great significance for understanding the process and mechanisms of failure during the experiment. Therefore, in the future, more advanced real-time visualization technology, data-driven and digital twin methods, and

other methods will be combined to conduct research on large-scale complex honeycomb sandwich structures.

**Author Contributions:** Conceptualization, W.S.; methodology, J.X. and X.H.; formal analysis, W.S. and B.H.; investigation, P.Z., H.Z. and J.X.; data curation, W.S., H.Z. and X.H.; writing—original draft preparation, W.S.; writing—review and editing, W.S., J.X., X.H., T.G. and K.T.; supervision, K.T.; funding acquisition, K.T. All authors have read and agreed to the published version of the manuscript.

**Funding:** This work was supported by National Key Research and Development Program project of China [No. 2022YFB3404700].

**Institutional Review Board Statement:** Not applicable.

**Informed Consent Statement:** Informed consent was obtained from all subjects involved in the study.

**Data Availability Statement:** Not applicable.

**Conflicts of Interest:** The authors declare no conflict of interest.

## References

- Seemann, R.; Krause, D. Experimental and numerical analysis of nomex honeycomb sandwich panel inserts parallel to the face sheets. In Proceedings of the 17th European Conference on Composite Materials, Munich, Germany, 26–30 June 2016.
- Qian, Z.Y.; Luo, W.B.; Yin, Y.Z.; Zhang, L.; Bai, G.; Cai, Z.; Fu, W.; Lu, Q.; Zhang, X.; Zhao, C. Dimensional stability design and verification of GF-7 satellite structure. *Chin. Space Sci. Technol.* **2020**, *40*, 10–17. [[CrossRef](#)]
- Wang, W.; Zheng, S.G.; Chang, J. Design and high velocity impact test verification of flexible space debris protection shield. *Chin. Space Sci. Technol.* **2019**, *39*, 82–86. [[CrossRef](#)]
- Bunyawanichakul, P.; Castanié, B.; Barrau, J.J. Experimental and numerical analysis of inserts in sandwich structures. *Appl. Compos. Mater.* **2005**, *12*, 177–191. [[CrossRef](#)]
- Bianchi, G.; Aglietti, G.S.; Richardson, G. Static performance of hot bonded and cold bonded inserts in honeycomb panels. *J. Sandw. Struct. Mater.* **2011**, *13*, 59–82. [[CrossRef](#)]
- Raghu, N.; Battley, M.; Southward, T. Strength variability of inserts in sandwich panels. *J. Sandw. Struct. Mater.* **2009**, *11*, 501–517. [[CrossRef](#)]
- Thomsen, O.T. Sandwich plates with ‘through-the-thickness’ and ‘fully potted’ inserts: Evaluation of differences in structural performance. *Compos. Struct.* **1997**, *40*, 159–174. [[CrossRef](#)]
- Demelio, G.; Genovese, K.; Pappalettere, C. An experimental investigation of static and fatigue behaviour of sandwich composite panels joined by fasteners. *Compos. Part B Eng.* **2001**, *32*, 299–308. [[CrossRef](#)]
- Yeh, H.Y.; Nguyen, S.V.; Yeh, H.L. Failure analyses of polymer matrix composite (PMC) honeycomb sandwich joint panels. *J. Reinf. Plast. Compos.* **2004**, *23*, 923–939. [[CrossRef](#)]
- Meng, L.B.; Jin, G.C.; Yao, X.F.; Yeh, H. 3D full-field deformation monitoring of fiber composite pressure vessel using 3D digital speckle correlation method. *Polym. Test.* **2006**, *25*, 42–48. [[CrossRef](#)]
- Guanchang, J.; Zhen, W.; Nikeng, B.; Xuefeng, Y. Digital speckle correlation method with compensation technique for strain field measurements. *Opt. Lasers Eng.* **2003**, *39*, 457–464. [[CrossRef](#)]
- Broggiato, G.B.; Newaz, G.M.; Amodio, D. Application of digital speckle correlation for strain measurement in composites. *Key Eng. Mater.* **2001**, *221*, 337–346. [[CrossRef](#)]
- Yao, X.F.; Meng, L.B.; Jin, J.C.; Yeh, H. Full-field deformation measurement of fiber composite pressure vessel using digital speckle correlation method. *Polym. Test.* **2005**, *24*, 245–251. [[CrossRef](#)]
- Peters, W.H.; Ranson, W.F. Digital imaging techniques in experimental stress analysis. *Opt. Eng.* **1982**, *21*, 427–431. [[CrossRef](#)]
- Chu, T.C.; Ranson, W.F.; Sutton, M.A. Applications of digital-image-correlation techniques to experimental mechanics. *Exp. Mech.* **1985**, *25*, 232–244. [[CrossRef](#)]
- Bruck, H.A.; McNeill, S.R.; Sutton, M.A.; Peters, W.H. Digital image correlation using Newton-Raphson method of partial differential correction. *Exp. Mech.* **1989**, *29*, 261–267. [[CrossRef](#)]
- Jin, G.C.; Yao, X.F.; Bao, N.K. Applications of speckle metrology to vibration and deformation measurements of electronic devices. In Proceedings of the Seventh Intersociety Conference on Thermal and Thermomechanical Phenomena in Electronic Systems (IEEE), Las Vegas, NV, USA, 23–26 May 2000.
- Zamani, M.H.; Heidari-Rarani, M.; Torabi, K. Optimal design of a novel graded auxetic honeycomb core for sandwich beams under bending using digital image correlation (DIC). *Compos. Struct.* **2022**, *286*, 115310. [[CrossRef](#)]

19. Giordano, A.; Mao, L.; Chiang, F.P. Full-field experimental analysis of a sandwich beam under bending and comparison with theories. *Compos. Struct.* **2021**, *255*, 112965. [[CrossRef](#)]
20. Li, X.; Yang, H.; Zhang, H.; Yin, L.; Zhang, Z.; Lei, H.; Fang, D. Failure mechanisms of fluted-core sandwich composite panels under uniaxial compression. *Compos. Struct.* **2023**, *303*, 116317. [[CrossRef](#)]

**Disclaimer/Publisher's Note:** The statements, opinions and data contained in all publications are solely those of the individual author(s) and contributor(s) and not of MDPI and/or the editor(s). MDPI and/or the editor(s) disclaim responsibility for any injury to people or property resulting from any ideas, methods, instructions or products referred to in the content.